Extending the luminescence properties of zinc gallogermanate via co-doping with cost-effective metals ions (Cr^{3+}/Mg^{2+}, Cr^{3+}/Ca^{2+}, and Cr^{3+}/Sr^{2+})

Moustafa M. S. Sanad[1,*] 🔘

[1] *Central Metallurgical Research & Development Institute, P.O. Box: 87, Helwan, Cairo, Egypt*

ABSTRACT

The huge applications of red-light-emitting materials paying the research attention to reduce the cost of production and raw materials. Therefore, abundant cations of alkaline-earth metals, e.g., Mg^{2+}, Ca^{2+}, and Sr^{2+} were successfully incorporated with Cr^{3+}: $Zn_3Ga_2Ge_2O_{10}$ (Cr-ZGGO) as co-activators via simple solid-state method. The X-ray diffraction results of all samples confirmed the formation of zinc gallogermanate superstructure with two cubic phases $ZnGa_2O_4$ and Zn_2GeO_4. The particle imaging of Cr-ZGGO and Ca@Cr-ZGGO via field emission scanning electron microscopy reveals a significant change in morphology and particle size by Ca^{2+} co-doping. Meanwhile, the energy dispersive X-ray spectroscopic analysis and mapping techniques elucidate the exact chemical composition of the calculated stoichiometric substitution and illustrate the equal distribution of all elements over the whole sample. Optical bandgap energy of Mg^{2+}, Ca^{2+}, and Sr^{2+} co-doped phosphors are lower than Cr-ZGGO. The Sr@Cr-ZGGO displays the most intense photoluminescence peak and the broadest emission in the near-infrared region as a result of increasing light traps and generation of new paths between the energy levels of trapping centers.

1 Introduction

The need for low-cost, highly stable and eco-friendly luminescent materials enforced the scientists to focus their research on metal oxide phosphors rather than metal sulfides [1]. Certain types of luminescent materials with long lasting phosphorescence are widely used in various applications such as optical imaging, light-emitting diodes and spectral converters [2–4]. It has been reported that Cr^{3+}-doped metal-based gallogermanate such as $La_3Ga_5GeO_{14}$, $Ca_3Ga_2Ge_4O_{14}$ and $Sr_3Ga_2Ge_4O_{14}$ displayed unique capabilities for near-infrared (NIR) emissions upon excitation with ultraviolet and visible light irradiation [5–7]. In recent years, zinc gallogermanate compounds have emerged as one of the most popular hosting materials to be applied for long persistent phosphors [8–10]. The reason for long red persistent

Address correspondence to E-mail: mustafa_sanad2002@yahoo.com

luminescence in $Zn_3Ga_2Ge_2O_{10}$ (ZGGO) as hosting material could be attributed to the presence of tetrahedral and octahedral sites available from the formed solid solution of two crystal structures, spinel $ZnGa_2O_4$ and willemite Zn_2GeO_4 [9, 11]. Therefore, single doping of ZGGO with Cr^{3+} or Mn^{2+} ions possessed red and green emissions as a result of $^2E \rightarrow {}^4A_2$ transitions caused by the lattice distortion in the octahedral positions [12–14]. Actually, the co-doping of Cr-ZGGO with Pr^{3+} was found to be an effective way to improve emissions performance up to 695 nm and prolong the afterglow properties especially at near-infrared region [15]. Similarly, the incorporation of Eu^{3+} in spinel Cr-ZGGO yielded a persistent NIR emission at 697 nm for in vitro bioimaging applications [16]. In addition, Lin et al. discovered that the co-doping of $Ca_3Ga_2Ge_3O_{12}$ with Nd^{3+} and Cr^{3+} would lower the energy transitions paths as a result of deeper traps generation between these energy levels achieving better and broader photoluminescence features [17]. Moreover, the photostimulation of spinel phosphors $Cr^{3+}:ZnGa_2O_4$ was clearly confirmed to achieve long persistent red emissions via complete or partial substitution of Zn^{2+} with Mg^{2+} [18, 19] and Ga^{3+} substitution with Sn^{4+} or Al^{3+} [20, 21]. This significant enhancement in these host luminescent materials could be attributed to the enlarged numbers of energy levels (i.e., crystal field splitting) which extend the trapping/de-trapping kinetics as a result of crystal structure distortion and the created vacancies in both octahedral and tetrahedral sites [22, 23]. Inspired by the previous concepts, this work suggests the substitution of Zn^{2+} in the ZGGO with different codopant ions Cr^{3+}/Mg^{2+}, Cr^{3+}/Ca^{2+}, and Cr^{3+}/Sr^{2+} to induce synergistic activation effects owing to the produced distorted spinel structure, cation vacancies and localized traps causing a strong red emission performance and significant delay for relaxation processes through a resonant energy transfer steps. Moreover, avoiding the utilization of rare earth activators such as (Eu^{3+}, Pr^{3+}, Nd^{3+}, etc.) and only use small portions of alkaline metals as co-activators will reduce the cost of these red phosphors. Hence, the present study aims at investigating the physicochemical, morphology, optical and photoluminescence properties of Cr^{3+}-doped ZGGO and their activated compounds with three types of earth abundant alkaline metals (Mg^{2+}, Ca^{2+}, and Sr^{2+}) in order to achieve high persistent red emission characteristics.

2 Experimental

2.1 Sample preparation

Pink powder samples of $Cr_{0.015}Zn_{2.985}Ga_2Ge_2O_{10}$ (Cr-ZGGO) and $M^{2+}_{0.015}$, $Cr_{0.015}Zn_{2.97}Ga_2Ge_2O_{10}$ ($M^{2+} = Mg^{2+}$, Ca^{2+}, or Sr^{2+}) were prepared via high temperature solid-state route. The starting materials for chemical synthesis are $Zn(CH_3CO_2)_2 \cdot 2H_2O$ (Fischer, 99%), Ga_2O_3 (Sigma-Aldrich, 99.99%), GeO_2 (MSE Supplies, 99.99%), Cr_2O_3 (Alfa Aesar, 99%), $Mg(CH_3COO)_2 \cdot 4H_2O$ (Sigma-Aldrich, 99.5%), $Ca(NO_3)_2 \cdot 4H_2O$ (Sigma-Aldrich, 99.99%), $Sr(NO_3)_2$ (Sigma-Aldrich, 99.99%). The stoichiometric mass of all components was placed together in a planetary ball mill to perform grinding at 400 rpm for 6 h. The ground powder then pre-calcined in muffle furnace at 800 °C for 2 h in air. The pre-calcined powders were subsequently calcined at 1200 °C for 6 h in air with heating rate 5°min^{-1}. The obtained four samples are ground again in an agate mortar for further physical and optical characterization.

2.2 Powder characterization

The crystal structure of the prepared samples was investigated using powder X-ray diffraction (XRD) of model Bruker AXS diffractometer (D8-ADVANCE Germany) with Cu Kα ($\lambda = 1.54056$ Å) radiation, operating at 40 kV and 40 mA in the 2θ range 20° and 60° and the scanning rate about 0.02°/0.4 s. The microstructure of the powder samples was disclosed by field emission scanning electron microscopy FE-SEM (JEOL-JSM-5410 Japan). The chemical analysis and elemental mapping were carried out by the energy dispersive X-ray spectrometer (EDS) Model: Apollo x attached with SEM with resolution 133 eV. Fourier transform infrared (FTIR) was employed for investigation using Jasco-6300 spectrometer (Japan) in the range 400–4000 cm^{-1}. The optical properties were tested using UV/VIS/NIR spectrophotometer (Model: Jasco-V-570, Japan) based on an integrating sphere reflectance unit in the wavelength range 250–1000 nm at room temperature. The fluorescence spectrophotometer (SHIMATDZU RF-5301PC Japan) was utilized to measure the photoluminescence emission peaks at room temperature after excitation of samples at $\lambda = 515$ nm with xenon discharge lamp of power ~ 150 W.

3 Results and discussion

3.1 XRD analysis

Figure 1a shows the XRD patterns of Cr-ZGGO; Mg@Cr-ZGGO; Ca@Cr-ZGGO and Sr@Cr-ZGGO powders calcined at 1200 °C for 6 h. The crystal structure of all samples reveals the formation of cubic superstructure of mixed spinel phase of $ZnGa_2O_4$ with JCPDS card no. 38-1240 and Zn_2GeO_4 with JCPDS card no. 25-1018. The hexagonal GeO_2 phase with JCPDS card no. 34-1089 is also detected as minor phase in Cr-ZGGO and Sr@Cr-ZGGO samples. However, it is associated with larger percentage in Mg@Cr-ZGGO and Ca@ZGGO samples. The slight shift in the diffraction peaks of ZGGO crystal planes at 111, 220, 311, 222, 400, 422, 511, 440, 620, 533, and 622 confirms the incorporation of Mg, Ca, and Sr in the ZGGO crystal structure due to change in the composition and stoichiometric properties as depicted in Fig. 1b. It is seen that the substitution with light elements (Mg and Ca) causes shift to lower angles, while the substitution with heavy element (Sr) shifts the XRD peaks to higher angles. Superstructure means two mixed phases forming one stable material in which the Ga-rich superlattice structures are stabilized by the stabilized in the substitution sites by

Ge lattices. The prepared ZGGO materials are considered a superstructure due to the high stability in the cubic crystal structure by replacing Ga with Ge atoms in their lattice sites. It is worth to note that all patterns that coincide with both $ZnGa_2O_4$ and Zn_2GeO_4 phases indicate the formation of zinc gallogermanate solid solution. The envisaged results are comparable to the reported XRD data in the literature [24–26]

3.2 SEM, EDS and elemental mapping

Figure 2a, b reveals the morphology of Cr-ZGGO particles which formed in large lumps with irregular shape and their main size was about 3–5 μm. Figure 2c indicates that Mg@Cr-ZGGO particles have larger grain size above 5 μm and smaller particles of GeO_2 (1–2 μm) are located between the grain boundaries and on the surface of large particles. Meanwhile, Ca@Cr-ZGGO sample appears with sphere-like morphology and smaller particle size about 1–3 μm suggesting that particle size homogeneity between zinc gallogermanate and germanium oxide compounds as shown in Fig. 2e. Figure 2g reveals Sr@Cr-ZGGO particles with 3 times larger size as a result of well crystal growth and stabilization of crystal lattice. The EDX analyses in
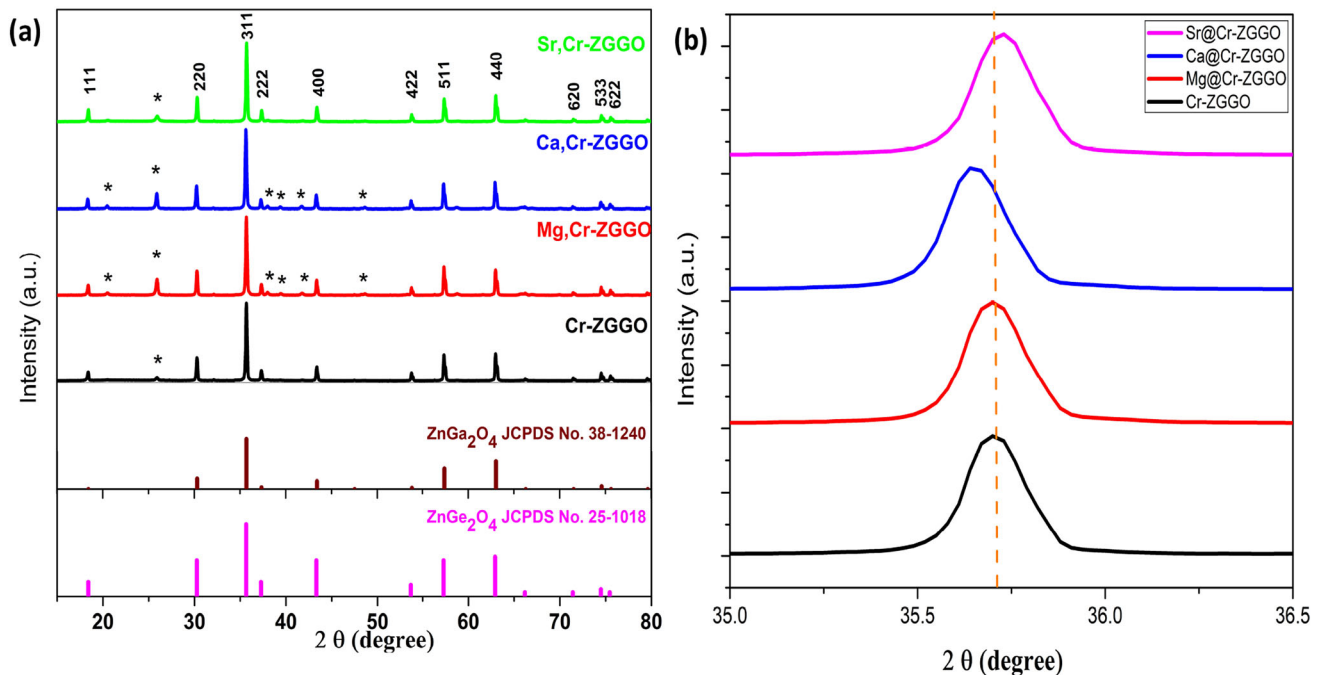

Fig. 1 a XRD diffraction patterns of Cr-ZGGO; Mg@Cr-ZGGO; Ca@Cr-ZGGO and Sr@Cr-ZGGO powders, (*) Hexagonal GeO_2 phase. **b** XRD peak shifting for alkaline metal-doped Cr-ZGGO samples
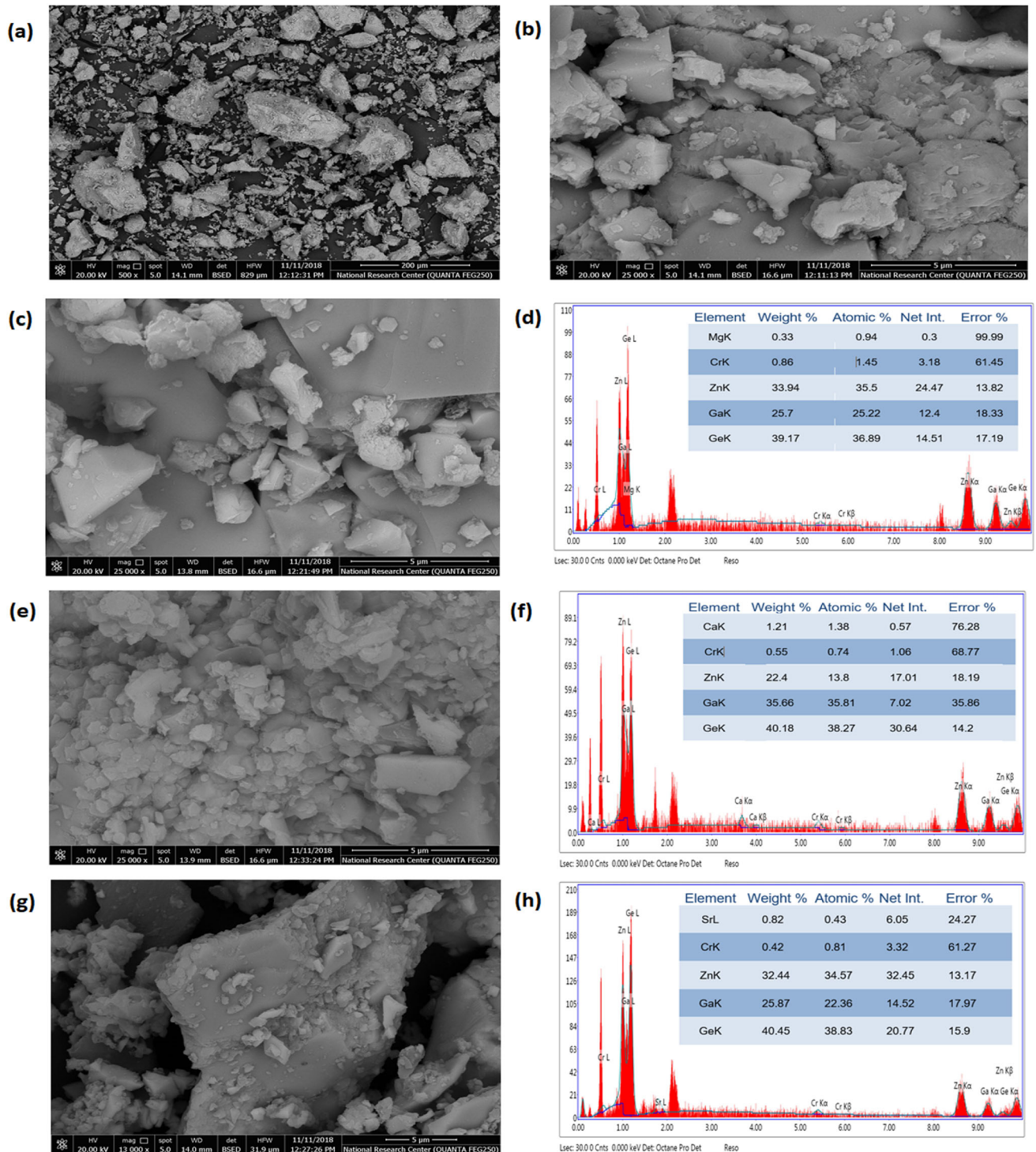
Fig. 2 SEM images of Cr-ZGGO sample at two magnifications (**a**, **b**), SEM and EDX analysis of Mg-doped Cr-ZGGO sample (**c**, **d**), SEM and EDX analysis of Ca-doped Cr-ZGGO sample (**e**, **f**), SEM and EDX analysis of Sr-doped Cr-ZGGO sample (**g**, **h**)

Fig. 2d, f and h illustrate the chemical compositions of Mg@Cr-ZGGO, Ca@Cr-ZGGO and Sr@Cr-ZGGO samples which confirm the actual weight percentage of each element which is very close to the calculated composition. Figure 3a–e shows the elemental mapping for Cr-ZGGO sample which indicates the uniform distribution of each element resulting in homogeneous solid solution of zinc gallogermanate.

Moreover, the EDS analysis in Fig. 3f reveals the actual chemical composition of Cr-ZGGO is approximately similar to the calculated formula. The observed morphology and particle size are in a good agreement with previously reported studies [27, 28].

3.3 FTIR analysis

Figure 4 reveals the FTIR absorption spectra of Cr-ZGGO and alkaline metal co-doped Cr-ZGGO samples. The broad and shallow absorption band observed around 300–3600 cm^{-1} in Cr-ZGGO sample could be assigned to the stretching vibration of O–H bonds in the absorbed water molecules [29]. The incorporation of Mg^{2+} and Sr^{2+} ions shifts this band to lower wave numbers due to the formation of secondary phase GeO_2, while the Ca^{2+} addition diminishes this absorption peak as result of crystal growth inhibition and formation of smaller crystals. The two weak absorption peaks at 2850 and 2920 cm^{-1} can be attributed to the stretching vibrations of C–H bonds [30]. The two overlapped peaks detected at 1500 and 1650 cm^{-1} are usually attributed to the bending vibrations of O–C=O and H–O–H bonds, respectively

[31]. Therefore, lower absorption and shift to higher wave numbers are noticeably occurred to these peaks by doping Cr-ZGGO with Mg^{2+}, Ca^{2+} or Sr^{2+} ions. This behavior could be explained by the enhanced crystallinity of the primary superstructure phase. The absorption bands in the range 750–900 cm^{-1} correspond to the stretching vibration modes of asymmetric metal–oxygen bonds such as Zn–O–Ga, Zn–O–Ge and Ga–O–Ge bonds where Mg@Cr-ZGGO and Sr@Cr-ZGGO possessed higher intense peaks than Cr-ZGGO and Ca@ZGGO samples [32]. Meanwhile, the two weak absorption bands at 480 and 610 cm^{-1} are assigned to the symmetric stretching vibrations of O–Ga–O/O–Ge–O and O–Zn–O bonds, respectively.

3.4 Optical and luminescence properties

3.4.1 Bandgap energy

The diffuse reflectance of the Cr-ZGGO and alkaline metal co-doped Cr-ZGGO samples were measured and converted to Kubelka–Munk function F(R∞) for calculation of optical bandgap according to the Tauc's law [33].
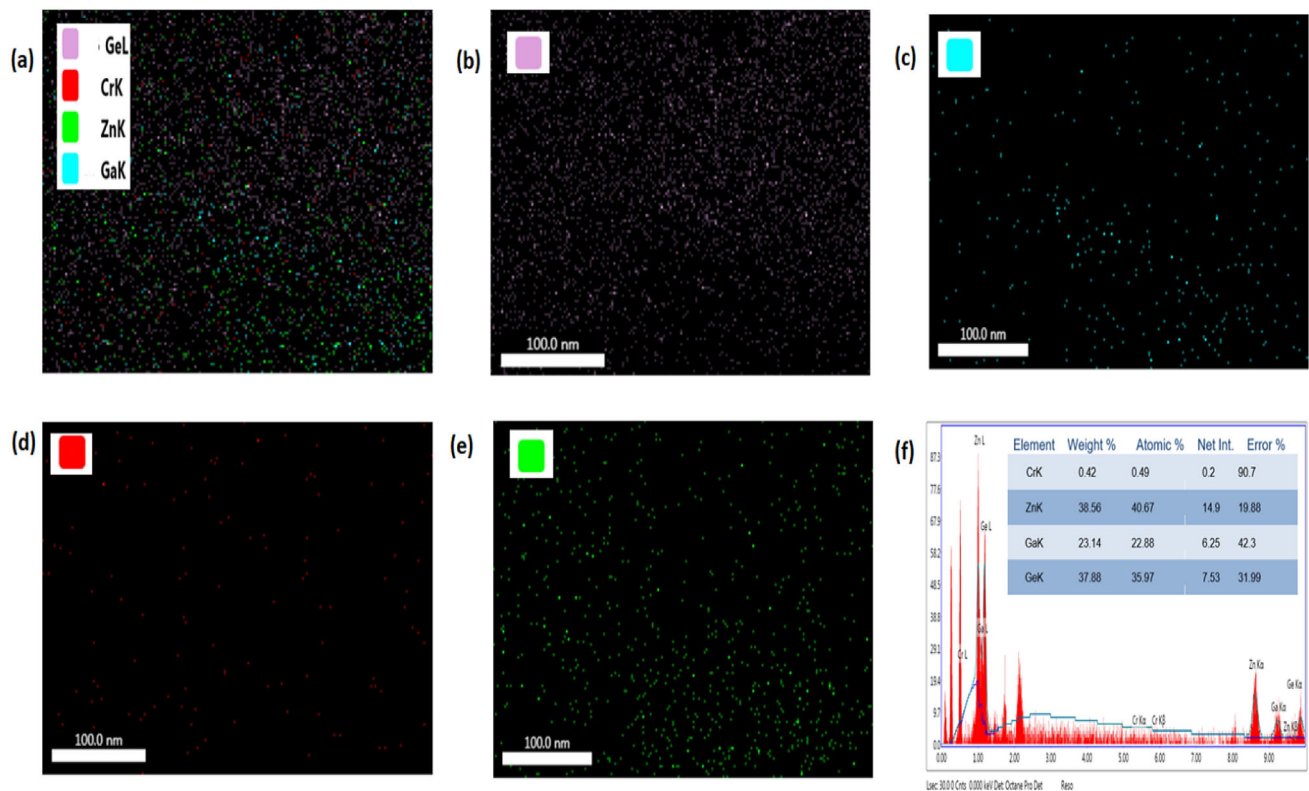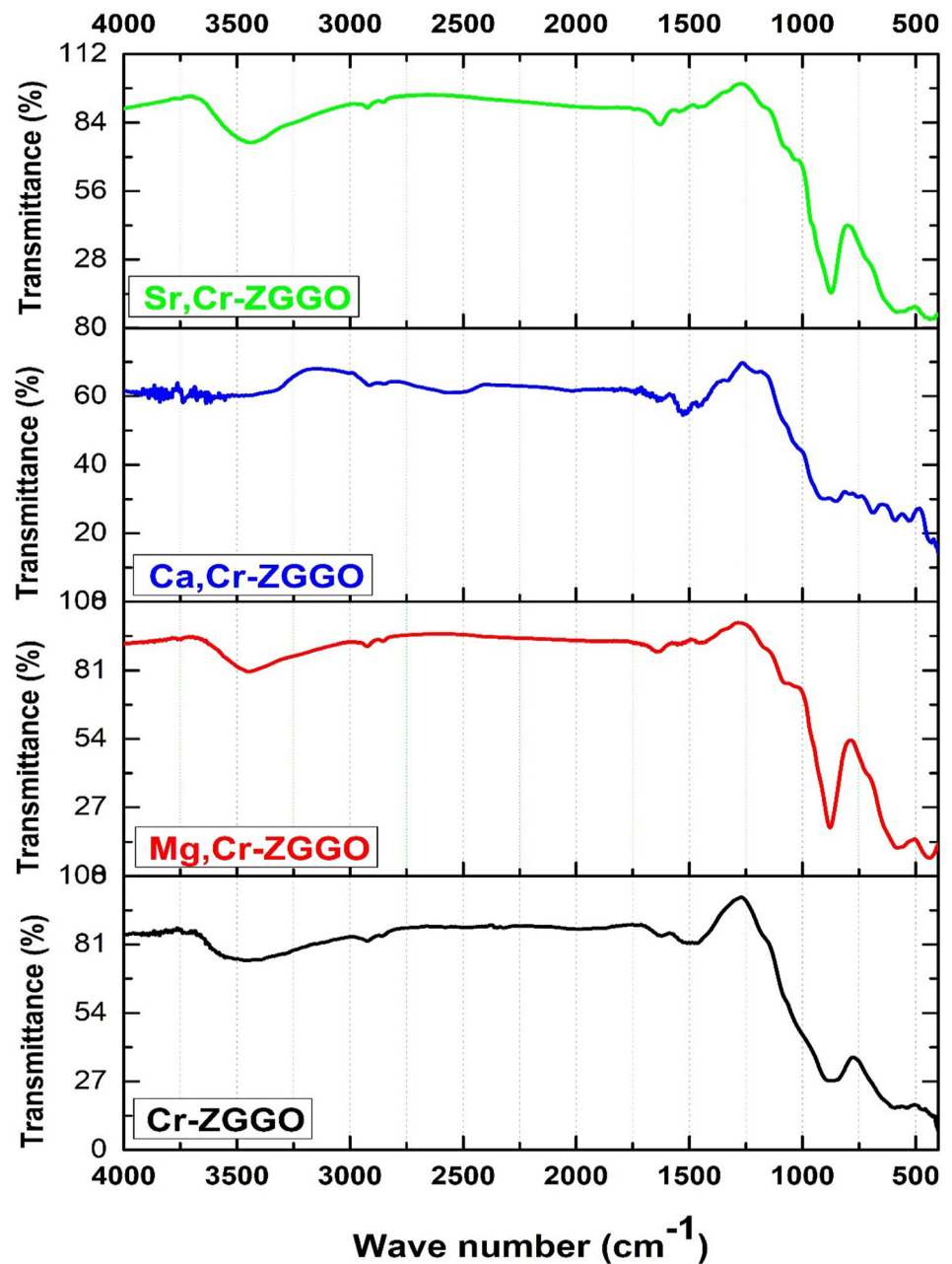

Fig. 3 a–e Elemental mapping of Cr-ZGGO sample, f EDX analysis of Cr-ZGGO sample

Fig. 4 FTIR absorption spectra of Cr-ZGGO and alkaline metal-doped Cr-ZGGO samples

$$[hv \times F(R\infty)]^2 = A \times (hv - E_g)$$

The bandgap values can be obtained from the intercept of the extrapolated straight line of $(\alpha hv)^2 - hv$ plot as shown in Fig. 5a–d. It is noticed that the bandgap energy (E_g) of Cr-ZGGO ~ 4.9 eV decreased by the additional doping with alkaline metals. The E_g values of about 4.2, 4.1 and 4.0 eV are found to be gradually decrease with increasing ionic radius of the alkaline metal according to the order Sr < Ca < Mg. The results are consistent with the

reported approach about Cr^{3+}-doped gallogermanate materials [34–36].

3.4.2 Photoluminescence properties

Figure 6a represents the produced emission spectra of Cr-ZGGO; Mg@Cr-ZGGO; Ca@Cr-ZGGO and Sr@Cr-ZGGO samples upon excitation at λ_{Ex} = 515 nm. The produced PL spectra for all samples appeared as broad peak with wavelength range 600–850 nm and band maxima at 697 nm. The
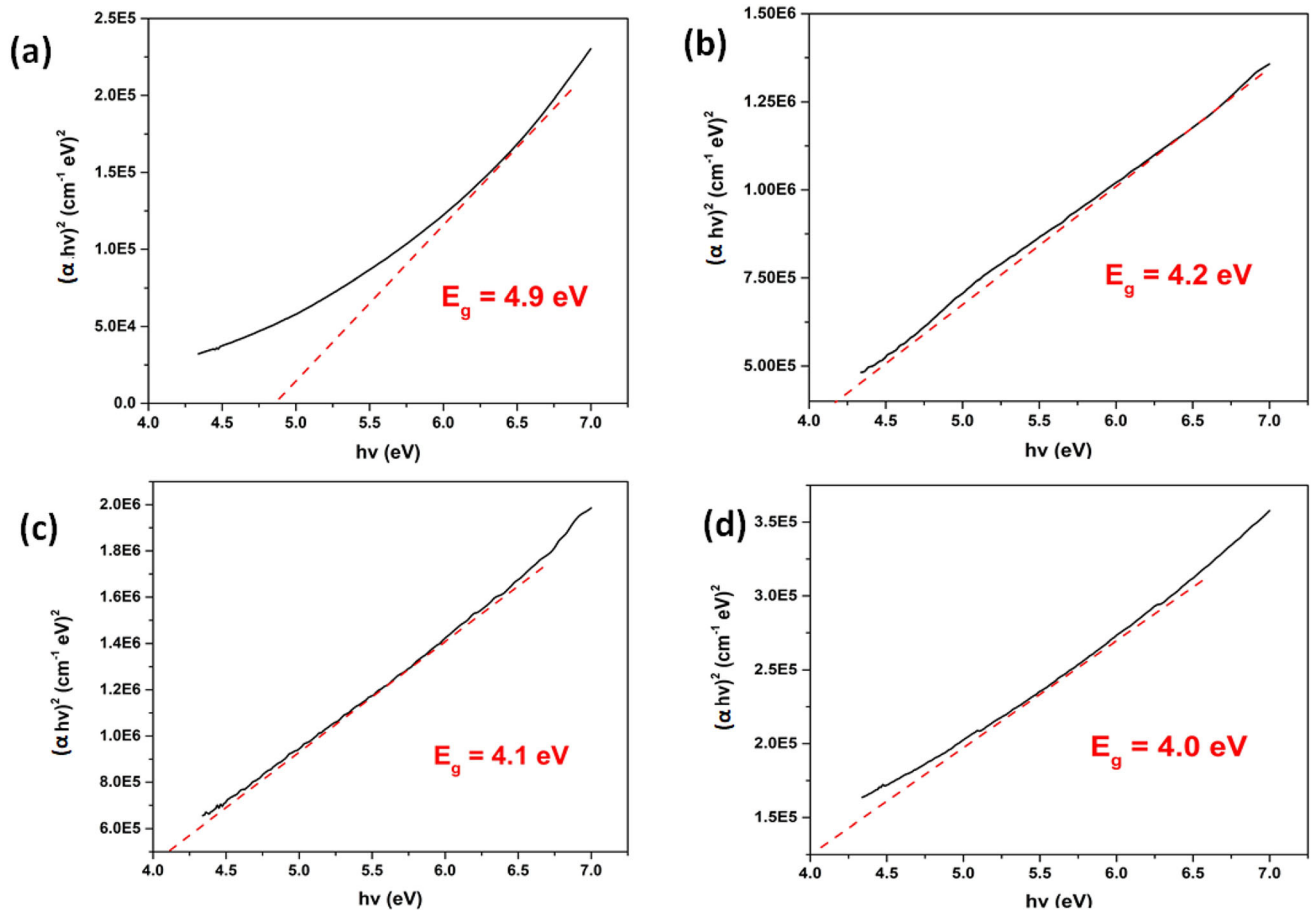
Fig. 5 Bandgap energy plots of Cr-ZGGO sample **a**, Mg@Cr-ZGGO sample **b**, Ca@Cr-ZGGO sample **c**, and Sr@Cr-ZGGO sample **d**

intensity and full width at half maximum (FWHM) of emission peaks are linearly increase with increasing ionic radius of the alkaline metal according to the order Sr < Ca < Mg as revealed in Fig. 5b. It is known that the Cr^{3+} introduction to ZGGO host compound creates sub-levels of energy states below the conduction band which act as trapping centers for enhancing the photoluminescence properties [28, 35, 37]. Accordingly, the incorporation of Mg^{2+}, Ca^{2+}, or Sr^{2+} is expected to increase the number of trapping levels which may enlarge the energy transfer from Cr^{3+} levels to Mg, Ca or Sr levels. These new energy transfer paths could clearly improve the photoluminescence response as previously discussed in the literature [17, 38]. It is worth to mention that the obtained PL results of Sr@Cr-ZGGO are better than previously reported results of Cr^{3+}/Pr^{3+} co-doped ZGGO [15].

4 Conclusion

The present work practically compared the employing of three types of alkaline-earth metals ($M^{2+} = Mg^{2+}$, Ca^{2+} or Sr^{2+}) as cheap co-activators in Cr-doped zinc gallogermanate red phosphors via simple solid-state pathway. The XRD results revealed the formation of mixed solid solution of two spinel phases, $ZnGa_2O_4$ and Zn_2GeO_4. The successful incorporation of Cr^{3+}/Mg^{2+}, Cr^{3+}/Ca^{2+}, and Cr^{3+}/Sr^{2+} was clearly elucidated using XRD, FE-SEM, EDS, and FTIR characterization tools. The Ca@Cr-ZGGO particles appeared with sphere-like morphology and particle size range about 1–3 μm, while Cr-ZGGO particles have non-distinct shape and larger particle size range about 3–5 μm. Both Mg@Cr-ZGGO and Sr@Cr-ZGGO samples exhibited FTIR absorption bands for Zn–O–Ga, Zn–O–Ge, and Ga–O–Ge bonds with higher intensity than Cr-ZGGO and Ca@ZGGO samples. Tauc's plot results indicated that the bandgap energy of Cr-ZGGO decreased by co-doping with
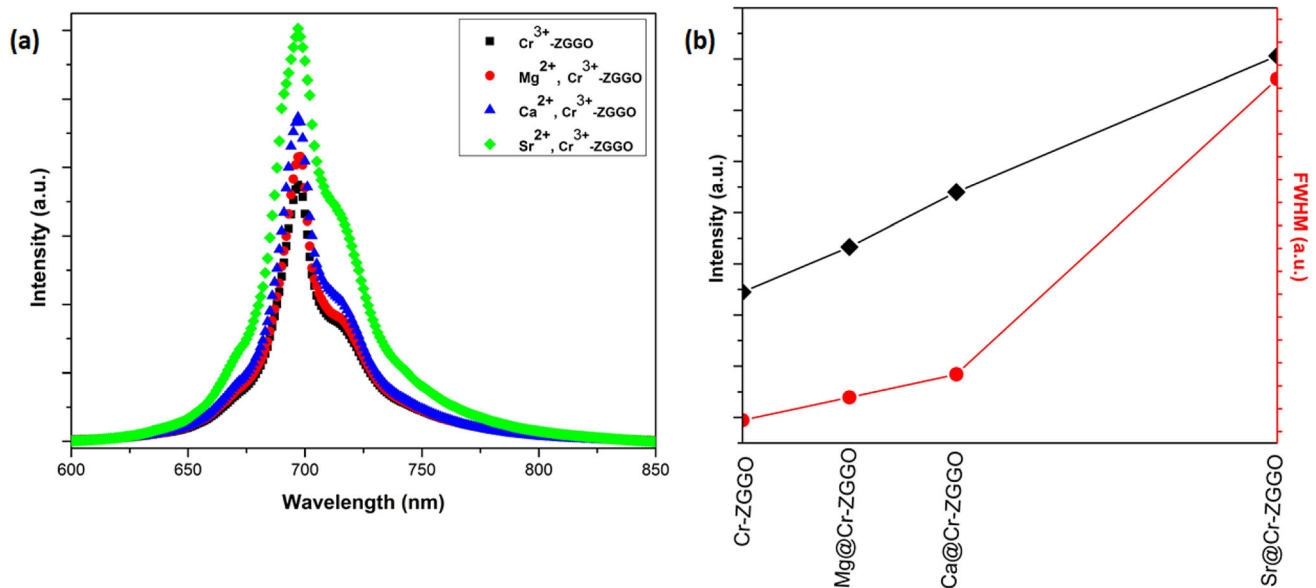
Fig. 6 **a** Photoluminescence spectra, **b** emission intensity and FWHM of Cr-ZGGO; Mg@Cr-ZGGO; Ca@Cr-ZGGO and Sr@Cr-ZGGO samples at excitation wavelength = 515 nm

Mg^{2+}, Ca^{2+}, and Sr^{2+} cations. All metal co-doped Cr-ZGGO samples showed improved photoluminescence characteristics due to generation of new energy transfer paths between the increased number of trapping levels resulting in persistent red-light emission.

Acknowledgements

References

1. R.E. Rojas-Hernandez, M.A. Rodriguez, F. Rubio-Marcos, A. Serrano, J.F. Fernandez, J. Mater. Chem. C **3**, 1268 (2015)
2. M.M.S. Sanad, D.A. Rayan, M.M. Rashad, Opt. Quant. Electron. **51**, 192 (2019)
3. M.M.S. Sanad, M.M. Rashad, J. Mater. Sci. Mater. Electron. **27**, 9034 (2016)
4. X. Huang, S. Han, W. Huang, X. Liu, Chem. Soc. Rev. **42**, 173 (2013)
5. W. Yan, F. Liu, Y.-Y. Lu, X.-J. Wang, M. Yin, Z. Pan, Opt. Express **18**, 20215 (2010)
6. P.I. Macfarlane, T.P.J. Han, B. Henderson, A.A. Kaminskii, Opt. Mater. **3**, 15 (1994)
7. A.A. Kaminskii, A.P. Shkadarevich, B.V. Mill, V.G. Koptev, A.A. Demidovich, Inorg. Mater. **24**, 579 (1988)
8. Z. Pan, Y.Y. Lu, F. Liu, Nat. Mater. **11**, 58 (2012)
9. M. Allix, S. Chenu, E. Véron, T. Poumeyrol, E.A. Kouadri-Boudjelthia, S. Alahraché, F. Porcher, D. Massiot, F. Fayon, Chem. Mat. **25**, 1600 (2013)
10. J. Ren, X. Xu, H. Zeng, G. Chen, C. Chen, D. Kong, Z. Liu, C. Gu, L. Kong, J. Am. Ceram. Soc. **97**, 3197 (2014)
11. T. Maldiney, A. Bessière, J. Seguin, E. Teston, S.K.S.B. Viana, A.J.J. Bos, P. Dorenbos, M. Bessodes, D. Gourier, D. Scherman, C. Richard, Nat. Mater. **13**, 418 (2014)
12. S.K. Singh, RSC Adv. **4**, 58674 (2014)
13. X. Xu, J. Ren, N. Huang, H. Zeng, G. Chen, D. Kong, C. Gu, C. Chen, Z. Liu, L. Kong, H. Tao, Opt. Mater. Express **4**, 2433 (2014)
14. X. Xu, J. Ren, G. Chen, D. Kong, C. Gu, C. Chen, L. Kong, Opt. Mater. Express **3**, 1727 (2013)
15. A. Abdukayum, J.-T. Chen, Q. Zhao, X.-P. Yan, J. Am. Chem. Soc. **135**, 14125 (2013)
16. Q. Wang, S. Zhang, Z. Li, Q. Zhu, Nanoscale Res. Lett. **13**, 64 (2018)
17. H. Lin, T. Yu, G. Bai, M.-K. Tsang, Q. Zhangb, J. Hao, J. Mater. Chem. C **4**, 3396 (2016)
18. N. Basavaraju, S. Sharma, A. Bessière, B. Viana, D. Gourier, K.R. Priolkar, J. Phys. D Appl. Phys. **46**, 375401 (2013)
19. M. Allix, S. Chenu, E. Véron, T. Poumeyrol, E. Kouadri-Boudjelthia, S. Alahraché, F. Porcher, D. Massiot, F. Fayon, Chem. Mater. **25**, 1600 (2013)

20. Y. Li, Y. Li, R. Chen, K. Sharafudeen, S. Zhou, M. Gecevicius, H. Wang, G. Dong, Y. Wu, X. Qin, J. Qiu, NPG Asia Mater. **7**, e180 (2015)

21. S.K. Sharma, D. Gourier, B. Viana, T. Maldiney, E. Teston, D. Scherman, C. Richard, Opt. Mater. **36**, 1901 (2014)

22. T. Maldiney, A. Lecointre, B. Viana, A. Bessiere, M. Bessodes, D. Gourier, C. Richard, D. Scherman, J. Am. Chem. Soc. **133**, 11810 (2011)

23. A. Bessiere, S.K. Sharma, N. Basavaraju, K.R. Priolkar, L. Binet, B. Viana, A.J.J. Bos, T. Maldiney, C. Richard, D. Scherman, D. Gourier, Chem. Mater. **26**, 1365 (2014)

24. Y. Wu, Y. Li, X. Qin, R. Chen, D. Wu, S. Liu, J. Qiu, Spectrochim. Acta Part A Mol. Biomol. Spectrosc. **151**, 385 (2015)

25. J. Ren, X. Xu, H. Zeng, G. Chen, D. Kong, C. Gu, C. Chen, Z. Liu, L. Kong, J. Am. Ceram. Soc. **97**, 3197 (2014)

26. J. Li, J. Shi, J. Shen, H. Man, M. Wang, H. Zhang, Nano-Micro Lett. **7**, 138 (2014)

27. A.C. Tas, J. Mater. Res. **17**, 1425 (2002)

28. F. Shen, C. Deng, X. Wang, C. Zhang, Mater. Lett. **178**, 185 (2016)

29. N. Kumam, N.P. Singh, L.P. Singh, S.K. Srivastava, Nanoscale Res. Lett. **10**, 347 (2015)

30. Y. Liu, D. Tu, H. Zhu, X. Chen, Chem. Soc. Rev. **42**, 6924 (2013)

31. T. Luan, J. Liu, X. Yuan, J.-G. Li, Nanoscale Res. Lett. **12**, 219 (2017)

32. T.A. Safeera, R. Khanal, J.E. Medvedeva, A.I. Martinez, G. Vinitha, E.I. Anila, J. Alloy. Compd. **740**, 567 (2018)

33. M.M.S. Sanad, A.M. Elseman, M.M. Elsenety, M.M. Rashad, B.A. Elsayed, J. Mater. Sci.: Mater. Electron. **30**, 6868 (2019)

34. N. Basavaraju, S. Sharma, A. Bessi'ere, B. Viana, D. Gourier, K.R. Priolkar, J. Phys. D: Appl. Phys. **46**, 375401 (2013)

35. Y. Zhuang, J. Ueda, S. Tanabec, P. Dorenbos, J. Mater. Chem. C **2**, 5502 (2014)

36. S. Yan, J. Wang, H. Gao, N. Wang, H. Yu, Z. Li, Y. Zhou, Z. Zou, Adv. Funct. Mater. **23**, 1839 (2013)

37. Q. Zhu, J. Xiahou, Y. Guo, H. Li, C. Ding, J. Wang, X. Li, X. Sun, J.-G. Li, A.C.S. Appl, Bio Mater. **2**, 577 (2019)

38. Y. Zhang, Z. Wu, D. Geng, X. Kang, M. Shang, X. Li, H. Lian, Z. Cheng, J. Lin, Adv. Funct. Mater. **24**, 6581 (2014)